Analysis and Control of Weapon Bay Flows

P. Nayyar, G. N. Barakos and K. J. Badcock

CFD Laboratory,

University of Glasgow

Glasgow, G12 8QQ

pnayyar@aero.gla.ac.uk

http://www.aero.gla.ac.uk/Research/CFD/projects/cavity/cavityflows.htm

Summary

Numerical analysis of the flow in weapon bays modelled as open rectangular cavities of length-to-depth (L/D) ratio of 5 and width-to-depth (W/D) ratio of 1 with doors-on and doors-off is presented. Flow conditions correspond to a Mach and Reynolds numbers (based on cavity length) of 0.85 and 6.783 million respectively. Results from Unsteady Reynolds-Averaged Navier-Stokes (URANS), Large-Eddy Simulation (LES) and Detached-Eddy Simulation (DES) are compared with the simulation methods demonstrating the best prediction of the complex flow. Results for a non-clean cavity (without doors) with a rear wall sting-mounted store are then presented to illustrate the effect of the missile on the cavity flow-field. The final part of the paper then demonstrates flow control of the cavity using passive control devices including the spoiler, slanted cavity walls and steady jet blowing with the jet proving to be the most effective in mitigating the noise level and frequency content inside the cavity.

1 INTRODUCTION

Modern high performance aircraft carry stores placed inside cavities embedded in the aircraft's fuselage. This implies that during store release phases of operation the aircraft will have to fly with the cavities exposed to the free-stream of air. During this phase, an unsteady, highly energetic flow-field can develop inside the cavity causing structural, acoustic and aerodynamic problems. Such flows have been investigated by Rossiter[1] in the 1960s at the Royal Aircraft Establishment who provided a first understanding of the phenomena. This was adequate for alleviating most of the problems encountered in the aircraft of that time. Recent designs, however, operate at more extreme conditions and have additional requirements for quieter operation and more lightweight structures. For this reason, aerospace engineers are revisiting the cavity flow problem to develop a better understanding of this complex flow and to improve their design methodologies.

In the 1980s, the high-speed aircraft of that time required more effective store carriage methods, especially at supersonic speeds, and internal store carriage again received attention. It was recognised that the internal carriage of missiles can cause large perturbations in the vicinity of the cavity, through which the missile must traverse and penetrate during launch. Most efforts undertaken to understand the separation and release characteristics of stores involved experiments[2–4] conducted at supersonic speeds and for shallow cavities with high aspect ratios. Although deeper cavities with low length-to-depth ratios (L/D) are known to exhibit more benign store release characteristics, the presence of the store can still influence the flow-field and hence alter the store release and separation characteristics. With Uninhabited Combat Aerial Vehicles (UCAVs) likely to play a significant part in future military aircraft designs, the need for store release at transonic speeds and with deeper weapons bays is still plausible.

The use of Computational Fluid Dynamics (CFD) for numerically analysing cavity flows has become more commonplace in the past decade. Accurate predictions of clean cavity flows are therefore important before more complex configurations including store release can be tackled. Some current research has looked at the simulation of cavity flows via methods such as Large-Eddy Simulation (LES)[5]. LES works by filtering the

flow structures in terms of scale size, with the larger scales explicitly resolved and the much smaller ones modelled using a sub-grid scale (SGS) model. With a significantly lower proportion of the flow modelled compared to Unsteady Reynolds-Averaged Navier-Stokes (URANS) methods, LES solutions are potentially more useful. For high Reynolds number flows, however, LES is expensive. Recent endeavours have therefore looked at developing hybrids of URANS and LES to obtain the best of both methods. One example of such developments includes the Detached-Eddy Simulation (DES), introduced by Spalart[6], which is currently available in many CFD solvers.

Although accurate prediction of cavity flows is of importance, the ultimate concern comes down to controlling the harsh aero-acoustic and turbulent cavity environment. Ever since the problems associated with cavity flows were recognised, many experiments and computations were conducted with the aim of improving the cavity environment. Some control methods involved manipulating the cavity geometry by either modifying the angle at which the cavity walls are slanted or by adding an external device to deliberately alter the flow inside the cavity. Such control techniques are referred to as passive, or open-loop, control because no feedback loop is used. Rossiter[1] and more recently Ross[7] have performed extensive wind tunnel experiments on the effectiveness of spoilers as one open-loop control device. The open-loop control methods are designed to be most effective at one particular stage in the aircraft's flight profile. Their limited versatility over a larger proportion of the flight envelope has, however, diverted attention toward closed-loop control methods, which continually adapt to the flight conditions making them more suitable for time-varying and off-design situations. Cattafesta *et al.* [8] provides an elaborate account of different open-loop and closed-loop control strategies adopted by different researchers.

This paper focusses on how CFD can be used for the analysis and control of the flow field inside a weapons bay, building on the experiments performed by Ross of QinetiQ[7]. The experiment considered a clean, open rectangular cavity with a length-to-depth ratio (L/D) of 5 and a width-to-depth ratio (W/D) of 1 with doors-on and doors-off. The flow conditions correspond to a Mach number of 0.85 and a Reynolds number of 6.783 million based on the cavity length. A variety of turbulence modelling and simulation techniques have been used, including LES and DES. Computations have been performed with the Parallel Multi-Block (PMB) code developed at the University of Glasgow[9].

Results are presented from URANS, LES and DES methods for both doors-off and doors-on cavity configurations. Comparisons were made with unsteady pressure measurements at the cavity floor[7] and with PIV measurements[10], and are discussed in detail in the following sections. The non-clean cavity configuration was then analysed with the aim of understanding the influence of stores on the 3D L/D=5, W/D=1 cavity with doors-off. As mentioned previously, the presence of stores can distort the flow-field inside the cavity and could cause adverse effects in the trajectory of stores during the initial phase of their release. A rear sting-mounted generic missile is placed inside the cavity to investigate this. The final part of the paper then looked at flow control of cavity flows. The effects of passive control devices such as the spoiler, slanted cavity walls and steady jet blowing were studied. This analysis forms part of a preliminary control study and so was conducted for the 2D, L/D=5 cavity using only the SST turbulence model, which, based on previous studies, provided reasonable accuracy on coarse grids.

2   MATHEMATICAL MODEL

2.1   CFD Solver

The Parallel Multi-Block (PMB) flow solver[9] solver has been successfully applied to a variety of problems including cavity flows, hypersonic film cooling, spiked bodies, flutter and delta wing flows amongst others. The code solves the unsteady Reynolds Averaged Navier-Stokes (RANS) equations on multi-block structured grids, in serial or parallel mode. Governing equations are discretised using a cell-centred finite volume method. The convective terms are discretised using either Osher's or Roe's scheme. MUSCL interpolation is used to provide nominally third order accuracy and the Van Albada limiter is used to avoid spurious oscillations across shocks. The time-marching of the solution is based on an implicit, dual time-stepping method. The final algebraic system of equations is solved using a Conjugate Gradient method, in conjunction

with Block Incomplete Lower-Upper factorisation. A number of turbulence models including one and two-equation statistical models as well as Large-Eddy Simulation (LES) and Detached-Eddy Simulation (DES) formulations have been implemented into the code. At the moment, the classical Smagorinsky Sub-Grid Scale (SGS) model is used to resolve the near-wall properties for LES while the one-equation Spalart-Allmaras and the two-equation $k - \omega$ and SST turbulence models are available for DES.

2.2 Turbulence Modelling

The SST turbulence model is typically presented as a 'blend' of the $k - \omega / k - \varepsilon$ models[11] but are phrased in $k - \omega$ form in PMB. The blended values for the model coefficients α, β, σ_k^{-1} and σ_ω^{-1} are given by

$$B \begin{pmatrix} a \\ b \end{pmatrix} \equiv F_1 a + (1 - F_1) b. \tag{1}$$

The blending function defined as

$$F_1 = \tanh \left(arg_1^4 \right), \quad arg_1 = min \left[\max \left(\frac{k^{1/2}}{\beta^* \omega y}, \frac{500 \nu}{y_n^2 \omega} \right), \frac{2 k \omega}{y_n^2 \max \left(\nabla k \cdot \nabla \omega, 0 \right)} \right]. \tag{2}$$

The SST model places an additional vorticity-dependent limiter on the shear stress, which is denoted as F_2:

$$F_2 = \tanh \left(arg_2^2 \right), \quad arg_2 = \max \left(\frac{2 k^{1/2}}{\beta^* \omega y}, \frac{500 \nu}{y^2 \omega} \right). \tag{3}$$

2.3 DES Formulation

Spalart[6] modified the one-equation Spalart-Allmaras model to achieve a DES equivalent. The only modification is in the dissipation term of the transport equation of $\tilde{\nu}$, given as

$$-C_{w1} f_{w1} \left(\frac{\tilde{\nu}}{\tilde{d}} \right)^2. \tag{4}$$

Originally,

$$\tilde{d} = d = \text{distance of the nearest wall} \tag{5}$$

whereas for DES, it is

$$\tilde{d} = C_{DES} \Delta \tag{6}$$

where C_{DES} is the DES coefficient and Δ is the metric of the grid size.

In practice, the following is employed

$$\tilde{d} = \min \left(d, C_{DES} \Delta \right), \quad \Delta = \max \left(\Delta_x, \Delta_y, \Delta_z \right) \quad \forall \quad \text{cell}, \tag{7}$$

although other metric relations are also possible.

The concept of employing a DES-like approach for turbulence models other than the one-equation Spalart-Allmaras was originally proposed by Strelets[12] and later by Batten & Goldberg[13]. For the two-equation $k - \omega$ model, for instance, the only modification, as with the one-equation Spalart-Allmaras DES variant, is in the dissipation term

$$-\beta^* \rho \omega k \tag{8}$$

The turbulent length scale is defined by

$$l = \frac{k^{1/2}}{\beta^* \omega} \tag{9}$$

Re-arranging for $\beta^* \omega$ and substituting into equation 8 gives

$$-\rho \frac{k^{3/2}}{l} \tag{10}$$

where l is given by

$$l = \min \left(l, C_{DES} \Delta \right). \tag{11}$$

C_{DES} is set to 0.78 and Δ is as before.

NATO/PFP UNCLASSIFIED

3 DESCRIPTION OF EXPERIMENTS BY ROSS *ET AL.*

Wind tunnel experiments conducted by Ross[7] at Aircraft Research Association Ltd (ARA) at Bedford, UK, were used for validation. The ARA wind tunnel is a 9 by 8 foot continuous flow, transonic wind tunnel (TWT) with ventilated roof, floor and side walls. Results for the doors-on configuration are compared with the corresponding experimental data (comparisons being made at several locations along the cavity floor as illustrated in Figure 1). Where 2D cavity results are mentioned, the comparison was made with the 3D clean cavity experimental case, where the bay doors were open vertically at 90°. The doors prevented any leakage at the cavity edges in the spanwise direction forcing the flow to channel into the cavity. In this configuration, the flow behaves as if it were 2D and is well represented by numerical modelling/simulation of a 2D cavity. Note that no experimental data was available for direct comparison with the numerical results obtained from the control study. Instead results were compared with experiment where no control device was used to illustrate the effectiveness of the control method.
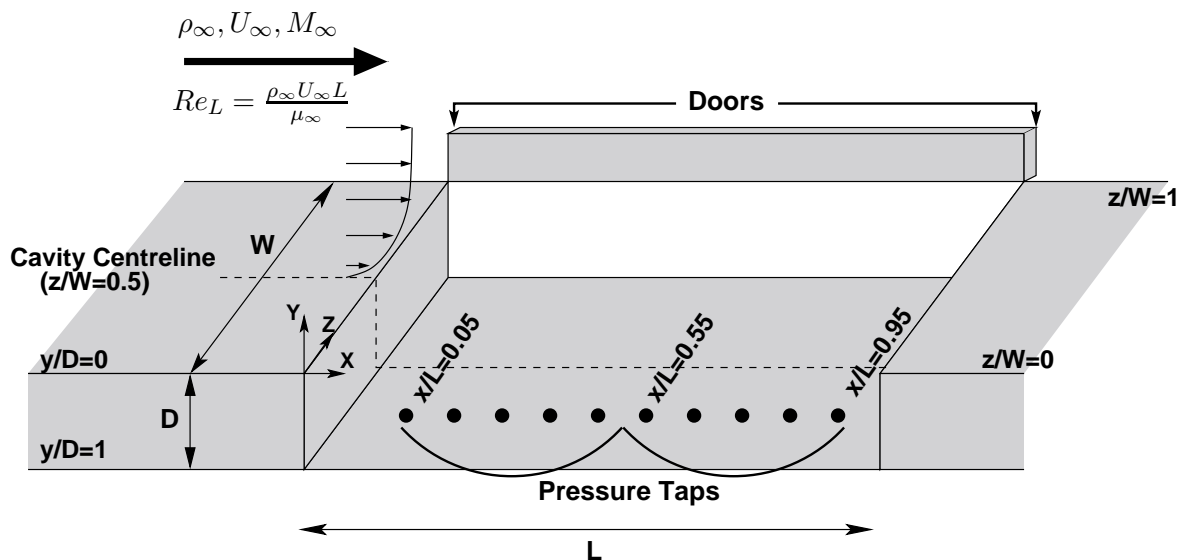
Figure 1: A schematic of the 3D, L/D=5, W/D=1 cavity (with doors-on) illustrating the positions of the pressure taps at which experimental and numerical results were compared.

The L/D=5 cavity model (with W/D=1) measured 20 inches in length, and 4 inches in width and depth. In the doors-on configuration, the doors were positioned at the front and rear walls in the z-direction and spanned the entire length of the cavity (see Figure 2(a)) and measured 0.375 inches width and 2 inches in height. The generic cavity rig model (designated as Model M219) was positioned at zero incidence and sideslip and the wind tunnel was operated at a Mach number of 0.85 and atmospheric pressure and temperature. Unsteady pressure measurements were registered inside and outside the cavity via Kulite pressure transducers: 10 pressure transducers were aligned along the centreline of the floor of the cavity rig, which was offset from the centreline of the actual cavity model (as shown in Figure 1), 2 on the flat plate ahead of the cavity, 1 on the flat plate aft of the cavity, 2 on the front and rear walls and 4 on the port side walls[7]. The data was sampled at 6000 Hz using a high-speed digital data acquisition system.

The measured data was presented in terms of Sound Pressure Level (SPL) and Power Spectral Density (PSD) plots. The SPLs are an indication of the intensity of noise generated inside the cavity and can be obtained from the measurements using the following equation:

$$\text{SPL (dB)} = 20 \log_{10} \left(\frac{\text{p}_{\text{rms}}}{2 \times 10^{-5}} \right) \tag{12}$$

where the p_{rms} is the RMS pressure normalised by the International Standard for the minimum audible sound of 2×10^{-5} Pa. Spectral analysis was performed using a Fast Fourier Transform (FFT) to obtain the power spectral density, which presents the RMS pressure versus frequency and is a measure of the frequency content inside the cavity.
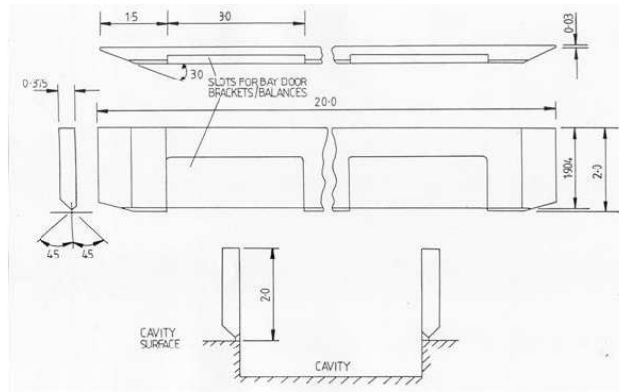
(a) Cavity Geometry
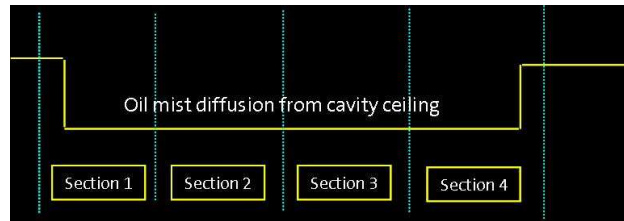
(b) PIV Experiment

Figure 2: Schematic of the wind tunnel cavity geometry (including the doors-on configuration) on the left and an illustration of the 4 different sections along cavity for which laser data acquisitions were taken with the PIV experiment on the right.

Measurements of the cavity flow-field were provided by PIV experiments conducted by Ross[10]. A stereoscopic two-camera system was employed for velocity measurements accompanied with a two-head Nd-YaG laser. Each laser pulse was fired within time intervals of 1μs. Four data acquisitions were taken with each acquisition comprising of 2 photographic images taken at 1μs intervals. The width of the laser sheet was limited to approximately 5.5 inches so the total cavity length of 20 inches was captured in 4 sections using motorised camera/laser traverse gear (Figure 2(b)). Seeding was provided by various combinations of water droplets sprayed in the settling chamber and vegetable oil mist diffusion from small holes in the cavity floor. Analysis of the data signals was performed by phase-locking onto each peak of signal and introducing a series of delays to synchronise image acquisitions at a particular part of the cycle. A number of acquisitions were then taken and averaged to define the flow-field at that part of the cycle. For highly unsteady flows with multiple cyclic components, it was recognised that phase-locking on any one component does not 'freeze' the flow-field. As highlighted by Ross[10], combined with the highly turbulent background, all aspects of a cavity flow are not likely to be accounted for. For a complete definition of the flow-field with time-dependency, very high-speed image acquisition equipment would be required.

4   RESULTS & DISCUSSION

The paper is split up into three parts. The first section compares results between the URANS, LES and DES for the clean cavity with and without doors. The next section addresses the non-clean cavity (without doors) with a rear wall sting-mounted missile inserted in the cavity shear plane. The final part then analyses results from the control study where the effects of the spoiler, slanted cavity walls and steady jet blowing as a passive control device are investigated. No experimental data was available for direct comparison with the CFD results for the non-clean cavity nor the flow control study. To illustrate the influence of the missile body on the cavity flow-field, comparisons were made with the experiment where no missile was used. Similarly

for the flow control study, comparisons were made with the experimental data where no control device was used, to illustrate the effectiveness of the control method.

4.1 Clean Weapon Bay Flow Analysis

The grids used in the numerical modelling and simulation of the empty weapons bay modelled as a clean 3D, L/D=5, W/D=1 open rectangular cavity are described in Table 1. All dimensions in these grids were scaled with respect to the cavity length. For the DES and LES grids, the far-field length was set to 3.5 times the cavity length so as to minimise any spurious results from acoustic wave reflections. A flat plate 1.5 times the cavity length (as in the experiment) was used ahead of the cavity to allow the oncoming boundary layer to develop naturally.

Grid Type	Pts. in Cavity (Overall)	Wall-Spacing	Blocks in cavity (Overall)
Clean cavity with doors-on (at 90°)			
3D URANS	446,824 (1,483,173)	1×10^{-5}	20 (110)
3D LES/DES (Coarse)	179,520 (1,248,544)	3.125×10^{-3}	64 (240)
3D LES/DES (Medium)	493,679 (2,218,854)	3.125×10^{-3}	64 (240)
3D LES/DES (Fine)	1,177,646 (4,783,162)	7.1825×10^{-4}	64 (240)
Clean cavity with no-doors			
3D URANS	305,424 (1,174,824)	2.214×10^{-5}	20 (110)
3D LES/DES (Coarse)	179,520 (1,225,824)	3.125×10^{-3}	64 (256)
3D LES/DES (Medium)	493,679 (2,178,480)	3.125×10^{-3}	64 (256)
3D LES/DES (Fine)	1,177,646 (4,696,128)	7.1825×10^{-4}	64 (256)
3D LES/DES (Very Fine)	2,097,152 (8,388,608)	5×10^{-5}	64 (256)

Table 1: Information on grids used for both the clean cavity in the doors-off and the doors-on at 90° configurations.

4.1.1 Doors-off Results

Comparisons from the clean, doors-off cavity for the URANS, DES and LES methods with unsteady pressure comparisons with experiment revealing best agreement with DES and LES (Figure 3(a)). URANS results were based on the coarse grid with Menter's Baseline $k - \omega$ model[11]. A time-step of 0.01 ($\equiv 1.814 \times 10^{-5}$s) was used for this computation — details of the grid are provided in Table 1. The fine grid was used for the DES computation with a time-step of 0.001 ($\equiv 1.814 \times 10^{-6}$s) and the very fine grid for the LES computation with the same time-step. The experimental signal was sampled at 6 kHz so the numerical results were sampled at the same rate for proper comparison.

The shape of the SPL curve for Menter's Baseline $k - \omega$ model still resembles the 'W' shape that is characteristic of the doors-on case, which will be discussed in greater detail in the following section (Figure 6(a)). Without doors, the flow inside and outside of the cavity is less constrained to move in the spanwise direction. The fact that Menter's Baseline $k - \omega$ model predicts a completely incorrect SPL shape (unlike LES and DES) suggests that it (and indeed URANS) has difficulty in accommodating effects of the greater transport and redistribution of energy and momentum in the spanwise direction. The difference in frequencies without the doors is clearly represented by the spectral analysis in Figure 3(b). The 3rd Rossiter mode (≈ 600 Hz) is more dominant for the doors-off cavity case compared to the 2nd mode (≈ 380 Hz) for the doors-on case. Although Menter's Baseline $k - \omega$ model predicts the 3rd mode relatively well, it fails to account for either the lower or higher frequencies. This is however not surprising since URANS can only account for the most energetic coherent structures in a flow. The 3rd Rossiter mode is the dominant frequency in the doors-off cavity configuration and so URANS captures this well but fails to account for any of the lower or higher frequencies.

Instantaneous Mach contours for both Menter's Baseline $k - \omega$ model and DES (with the one-equation Spalart-Allmaras model) along the cavity centreline are illustrated in Figure 4. The Mach number plots

(a) SPLs

(b) PSD ($x/L = 0.95$)
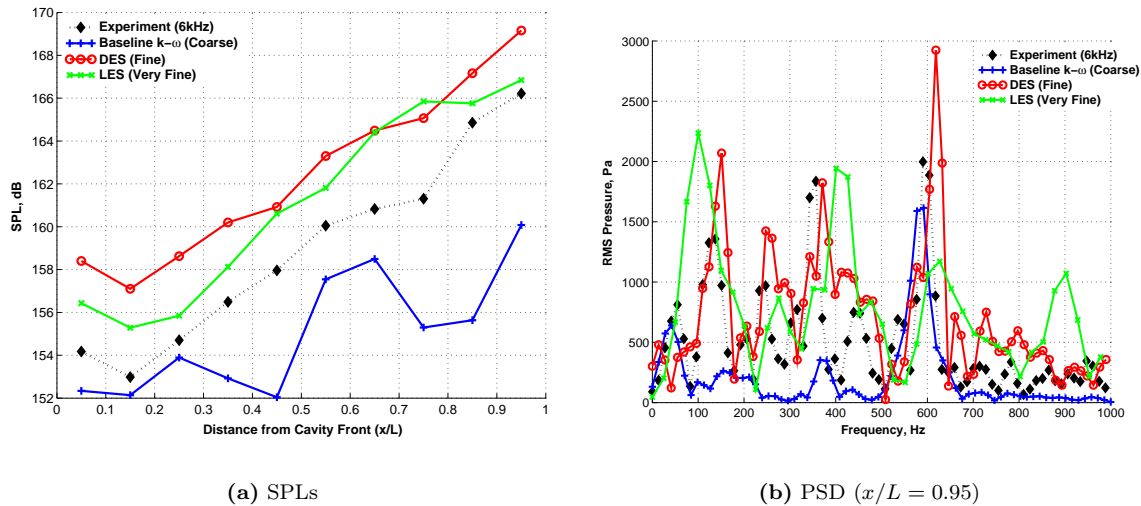
Figure 3: SPL and PSD plots (at $x/L = 0.95$) for the 3D, L/D=5, W/D=1, clean cavity with doors-off using the coarse grid for URANS (with Menter's Baseline $k - \omega$ model), fine grid for DES (with Spalart-Allmaras model) and very fine grid for LES (with Smagorinsky SGS). Plots taken at z/W=0.25 and along the cavity floor (y/D=1).

distinctly demarcate the lower-velocity regions (blue) inside the cavity from the transonic regions (yellow) outside the cavity. Where these two regions coalesce is where the shear layer is located. Menter's Baseline $k - \omega$ model always predicts a larger single primary vortex structure at the cavity rear with some combination of two or more counter-rotating vortices at the cavity front. The shear layer is also consistently found to span the cavity with distinct deflection at the cavity rear (Figure 4). It is this dual-vortex cycle inside the cavity that results in the 'W'-shaped SPL curve in Figure 3(a). The difference between the DES and URANS flow-field results lies in the behaviour of the shear layer and this is evident in Figure 4. At no point for the DES computations does the shear layer extend across the entire length of the cavity. At the most, the shear layer can be observed to be coherent up to the middle of the cavity at which point, if not earlier, it breaks down. What follows is intensive mixing and spreading of the energy from the shear layer and the free-stream with the lower-velocity flow region inside the cavity. The pressure at the cavity rear rises due to this mixing process and is manifested in the form of a rising SPL curve (Figure 3(a)).

With the shear layer detached, the flow within the cavity is no longer entrained within it and large vortical structures can no longer be sustained. More turbulence, higher frequencies and smaller vortices instead form. These interact with the cavity walls to create regions of higher pressure and more flow activity. Not confined by the shear layer, the flow can now be observed to 'spill' over the cavity in both the streamwise and spanwise directions. Indications of these 'spillages' can be distinctly seen in LES and, to a lesser extent, LES computations in Figure 5, which provides a three-dimensional perspective of the instantaneous flow field (using Mach contours normalised by the free-stream Mach number of 0.85) inside the 3D clean cavity in the doors-off case. As URANS does not predict the breakdown of the shear layer, these vortical 'spillages' are also not observed in URANS computations.

4.1.2 Doors-on Results

Figure 6 shows the difference between the DES, LES and URANS methods in the prediction of noise levels and frequencies for the clean, doors-on cavity configuration. The coarse grid was used with Menter's Baseline $k - \omega$ model for URANS computations with a time-step of 0.01 ($\equiv 1.814 \times 10^{-5}$s), the fine grid for the DES computation with a time-step of 0.001 ($\equiv 1.814 \times 10^{-6}$s) and the medium grid for the LES computation with a time-step of 0.005 ($\equiv 9.07 \times 10^{-6}$s). Due to the success of the DES with the one-equation Spalart-Allmaras turbulence model for the doors-off case, it was decided to run a fine grid computation using DES rather
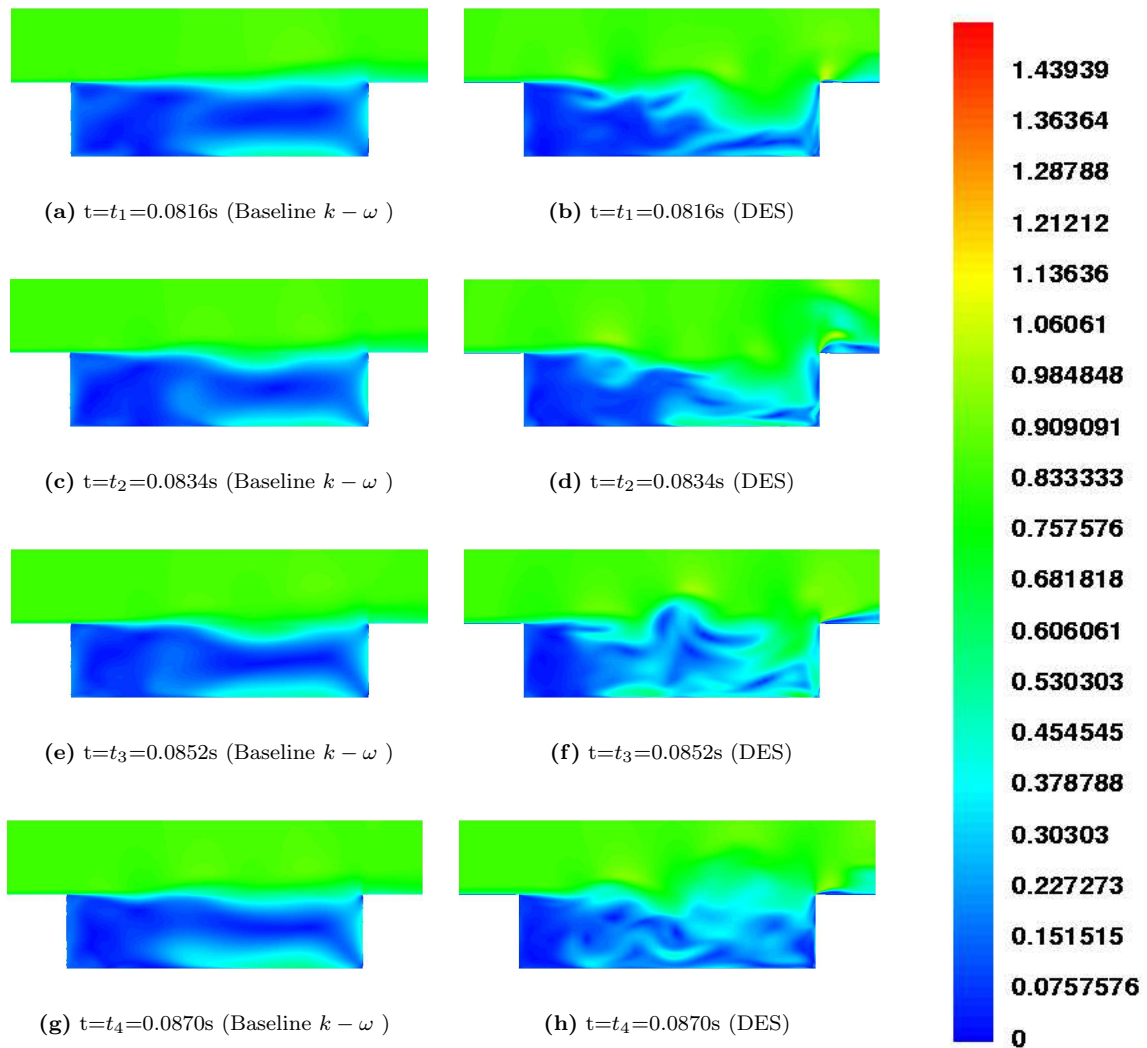
Figure 4: Instantaneous Mach contours with streamlines for the clean cavity with no-doors illustrating flow features inside the 3D cavity at for 4 different time-steps during flow cycle for the coarse URANS (Menter's Baseline $k - \omega$ turbulence model) and fine DES (one-equation Spalart-Allmaras turbulence model) computations. Plots taken along the cavity centreline (z/W = 0.5).

than using very fine grids with LES. Two sets of unsteady pressure experimental data were available for the doors-on case: one was sampled at 6 kHz and another with a higher sampling rate of 31.25 kHz. Both of these experimental data sets are included in Figure 6 to emphasise the importance of high resolution experimental data. All numerical results were sampled at 31.25 kHz.

Menter's Baseline $k - \omega$ turbulence model was used for URANS while the one-equation Spalart-Allmaras model was used with DES to realise the turbulent near-wall properties. Variations in SPLs across the cavity length along its floor is illustrated in Figure 6(a). All three methods agree reasonably well with experiment, with URANS agreeing even better with experiment in some cases. Near the front of the cavity, for instance, the shape of the SPL curve for Menter's Baseline $k - \omega$ model follows the experiment better than the DES and LES counterparts.

A closer inspection of the frequency content at the cavity rear ($x/L = 0.95$) illustrates a less satisfactory agreement between Menter's Baseline $k - \omega$ model and experiment (Figure 6(b)). Neither the 1st (≈ 160 Hz) nor the 3rd (≈ 600 Hz) Rossiter modes are captured. The 2nd Rossiter mode (≈ 400 Hz) is well captured but is over-predicted by about 1 kPa. This over-prediction was found to be a common occurrence for most

(a) Baseline $k - \omega$ **(b)** DES

(c) LES
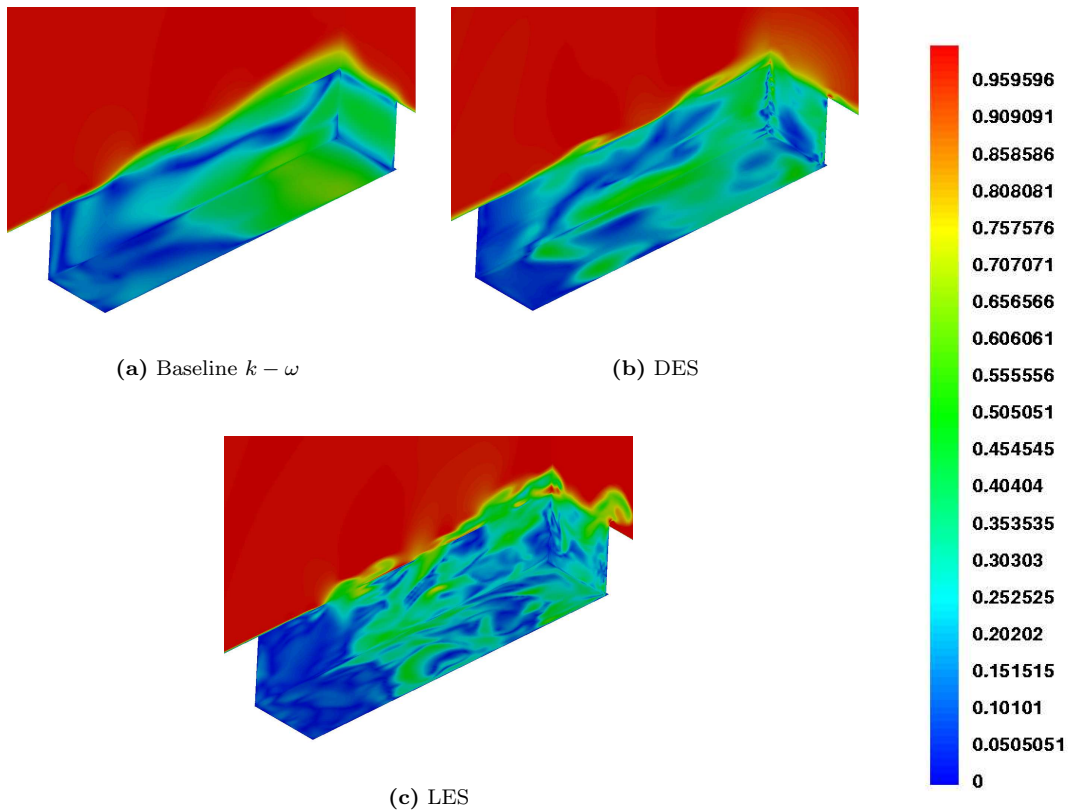
Figure 5: Three-dimensional perspective of the flow field inside the 3D L/D=5 clean cavity with doors-off for the URANS (with the Menter's Baseline $k - \omega$ model), DES (with the one-equation Spalart-Allmaras model) and LES (with the classical Smagorinsky SGS) methods. Plots show instantaneous Mach contours normalised by the free-stream Mach number of 0.85.

URANS comparisons with experiment.

4.1.3 PIV Comparisons

PIV data was provided by Ross[10], as described above. The PIV experiment was conducted for the 3D cavity in the doors-on configuration only and so results from the corresponding doors-on computations are only compared with it.

Streamwise and transverse velocity profiles for three different stations inside the cavity (x/L=0.05, x/L=0.55 and x/L=0.95 - see Figure 1 for the positions of these pressure taps) for both DES and LES computations are illustrated in Figure 7. The black line denotes the PIV results. The three other plots included in the velocity profile plot correspond to the time-averaged DES results with the one-equation Spalart-Allmaras model (solid green line), DES results with the two-equation $k - \omega$ model (dashed red line) and LES results with the classical Smagorinsky sub-grid scale model (dashed-dot blue line) for the coarse grid (refer to Table 1 for information on the grids used) at a time-step of 0.01 ($\equiv 1.814 \times 10^{-5}$s). The results are encouragingly consistent for both DES variants and LES.

Agreement with PIV is, however, sensitive to the station analysed. At the first two stations, at x/L=0.05 (cavity front) and at x/L=0.55 (cavity middle), the agreement between DES, LES and PIV is good. At the cavity rear (x/L=0.95), agreement with PIV deteriorates. The explanation for this may lie in the manner in which the PIV experiment was conducted. As mentioned previously, the laser used for the PIV experiment had a width of approximately 5.5 inches, which is roughly equivalent to a quarter of the cavity length. The laser was fired at four different sections in order to cover the entire length of the cavity (Figure 2(b)). The

(a) SPLs

(b) PSD ($x/L = 0.95$)
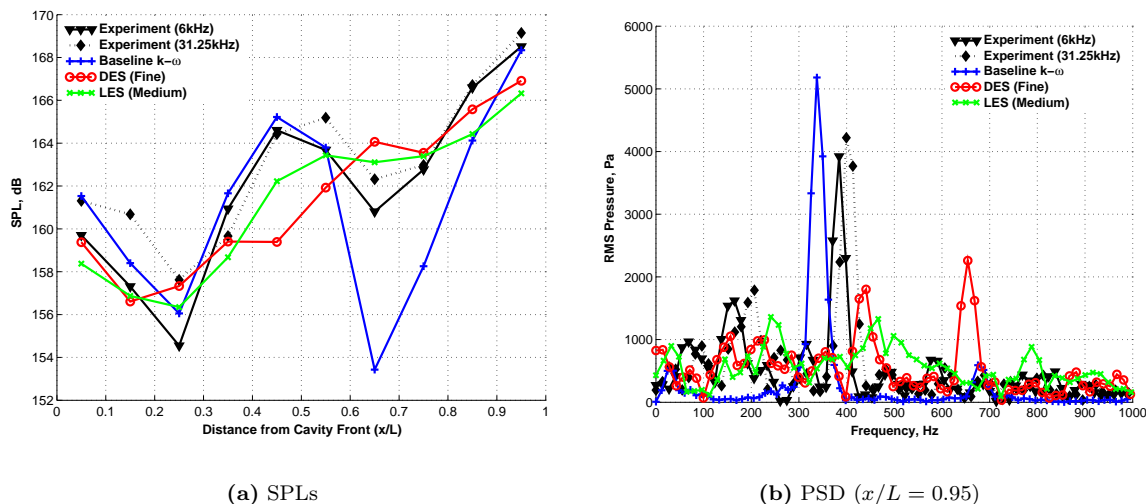
Figure 6: SPL and PSD plots (at $x/L = 0.95$) for the 3D, L/D=5, W/D=1, clean cavity with doors-on at 90° vertically with the coarse URANS grid (Menter's Baseline $k - \omega$ turbulence model), fine DES grid (with Spalart-Allmaras model) and medium LES grid (with Smagorinsky SGS). Plots taken at z/W=0.25 and along the cavity floor (y/D=1).

resolution of the PIV experiment was found to be good at the first two stations that the computational results were analysed at, i.e. at x/L=0.05 and x/L=0.55, but was not at the third station, i.e. at x/L=0.95. This is illustrated in Figure 8, which indicates the variations in the streamwise and transverse velocity components along the length of the cavity for the PIV experiment at a distance equal to the depth of the cavity above the cavity lip.

The experiment was conducted at a Mach number of 0.85 and a freestream velocity of 296 m/s. In sections 1 and 3 of the PIV experiment, which are where the first two stations x/L=0.05 and x/L=0.55 respectively lie, the laser resolution is good and the streamwise velocity is close to its anticipated value of 296 m/s (Figure 8(a)). In section 4, however, which is where the third station x/L=0.95 lies, the resolution deteriorates and the streamwise fluctuations are significantly larger. A consistent story is told by the transverse streamwise plots in Figure 8(b). This possibly explains the discrepancies between the LES, DES and PIV data at the cavity rear. This also further emphasises the problems with using PIV for highly unsteady flows at high Mach and Reynolds numbers. As mentioned by Ross[10], higher imaging and data acquisition equipment is likely to be required for consistently good resolution throughout the cavity cross-section.

4.2 Weapon Bay Flow with Stores

Results for a 3D, L/D=5, W/D=1 cavity are presented with a missile placed along the shear layer plane (i.e. y/D=0) of the cavity (refer to Figure 1 for details of the cavity frame of reference). The store corresponds approximately to the size of an air-to-air missile and is sting-mounted at the rear of the cavity. Two configurations for the missile are intended to be investigated and these involve using the missile with and without fins. For the case where no fins are attached to the missile, two further modes of analyses were performed: one with the half-model cavity and the other with a full representation of the missile and the cavity. This approach also allows justification of the symmetry boundary condition assumption applied at the cavity half-width for the half-model configuration. Details of the different grids used for the cavity with missile study are given in Table 2 below.

No experimental data was available for the cavity with the missile configuration so numerical results were compared with the experimental data where no missile was placed inside the cavity to illustrate the effect of the missile. In addition, numerical results from the 8.5 million point LES grid (with doors-off) are also included for reference. Where the cavity without any missile is referred to, it is denoted as 'baseline'.

Profile located within Section 1 of Figure 2(b)
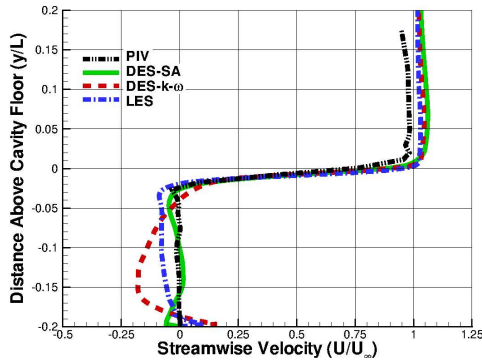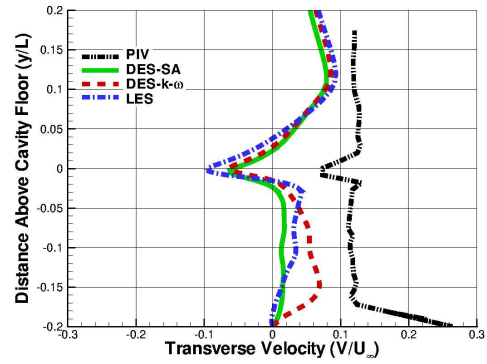
(a) U-Velocity (x/L=0.05)

(b) V-Velocity (x/L=0.05)

Profile located within Section 3 of Figure 2(b)
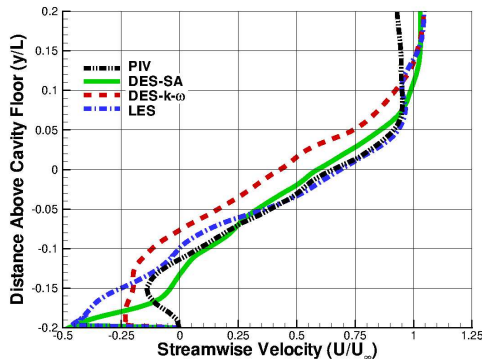
(c) U-Velocity (x/L=0.55)
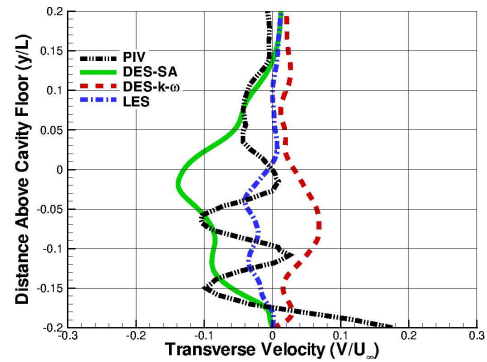
(d) V-Velocity (x/L=0.55)

Profile located within Section 4 of Figure 2(b)
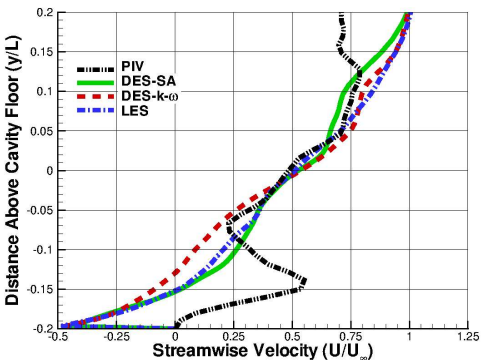
(e) U-Velocity (x/L=0.95)

(f) V-Velocity (x/L=0.95)

Figure 7: Time-averaged streamwise ($\frac{U}{U_\infty}$) & transverse ($\frac{V}{V_\infty}$) velocity profiles for the clean cavity with doors-on at 3 locations along cavity floor at x/L=0.05, x/L=0.55 and x/L=0.95 with coarse grids and a CFD time-steps of 0.01 ($\equiv 1.814 \times 10^{-5}$s) for DES computations with Spalart-Allmaras (green) and $k - \omega$ (red) models. LES results are denoted by the blue line. Black Line corresponds to experimental PIV data (provided by Ross[10]).

For the missile without fins, the computational domain for a half-model cavity with a half-model missile placed on the cavity's shear layer plane at its half-width position (i.e. z/W=0.5) was generated. A symmetry boundary condition was applied across the cavity half-width position. The full-model cavity was generated
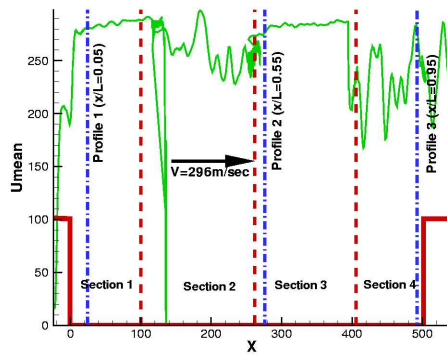
(a) PIV Streamwise (U) Velocity
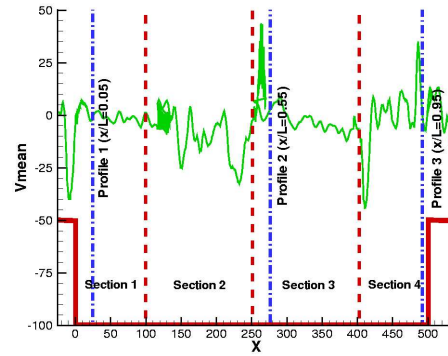
(b) PIV Transverse (V) Velocity

Figure 8: Streamwise & transverse velocity traces at a distance equal to the depth of the cavity above the cavity lip.

Grid Type	Pts. in Cavity (Overall)	Wall-Spacing	Blocks in cavity (Overall)
Clean Cavity without Missile			
Clean LES (Very Fine)	2,097,152 (8,388,608)	5×10^{-5}	64 (256)
Cavity with Missile (With Fins)			
Half-Missile LES (Medium)	772,410 (2,497,680)	1×10^{-5}	54 (166)
Cavity with Missile (Without Fins)			
Half-Missile LES (Coarse)	147,500 (767,250)	1×10^{-5}	17 (61)
Half-Missile LES (Medium)	407,200 (1,648,800)	1×10^{-5}	17 (61)
Full-Missile LES (Fine)	976,800 (3,876,000)	1×10^{-5}	17 (61)

Table 2: Information on grids used for the missile with and without fins placed in the shear layer plane of the L/D=5, W/D=1 cavity in the doors-off configuration.

simply by mirroring this grid about the symmetry axis. Figure 9 provides a view of the mesh distribution on and around the missile (without fins) and the surrounding symmetry plane.
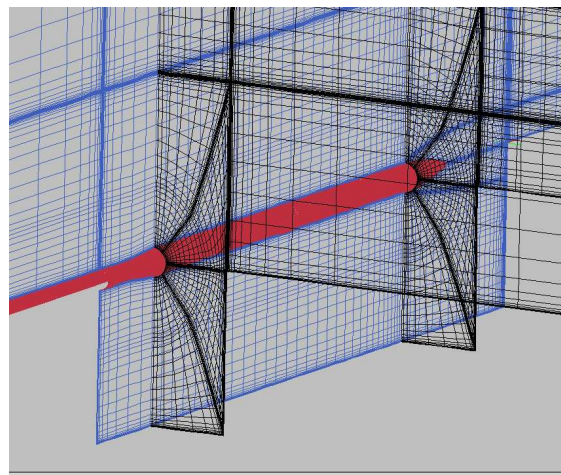
Figure 9: Mesh distribution on and around the half-body missile without fins.

Initial results for the half-model missile without fins were attempted on a very coarse grid by LES standards. Although subsequent grids were finer and the full missile grid approached 4 million points, the resolution of these grids is admittedly low for LES computations. However, previous analyses of cavity flows using LES [14] have however revealed good and consistent agreement with experiment even with relatively low resolution grids. As a first understanding of the flow inside the cavity with a store, the results presented should therefore hold reasonable merit.

Analysis of the noise level content along the cavity floor is shown in Figure 10, which also includes the pressure signature at the cavity rear ($x/L = 0.95$). Comparisons are made among LES results obtained for the half-body missile coarse (depicted by the red lines with circular symbols) and medium (shown by the green lines with crosses) grids and the full-body missile grid (denoted in magenta lines with square symbols). Experimental and numerical results (indicated by the black lines with diamond symbols and blue lines with plus signs, respectively) correspond to the clean cavity with no missile. SPLs for the full-body missile are about 2 to 10 dB lower from the baseline results.

(a) Pressure Traces ($x/L = 0.95$)

(b) SPL
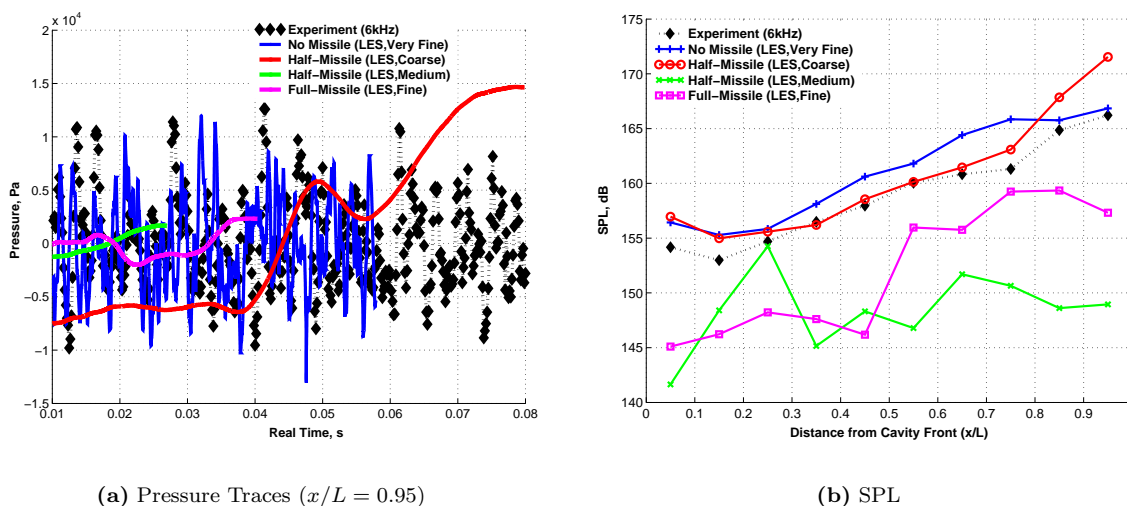
Figure 10: SPLs and pressure traces at cavity rear ($x/L = 0.95$) along the cavity floor for the 3D, L/D=5, W/D=1 cavity with missile without fins using LES for the coarse and medium half-body missile grids and the fine full-body missile.

The noise level produced for the half-body missile is generally higher than the full-body missile and is of the same order of magnitude as the baseline results. This is particularly evident with the half-body coarse grid missile result (Figure 10(b)). It would therefore seem that the symmetry boundary condition applied for the half-body missile is an incorrect assumption, despite the geometrical symmetry.

Band-limited SPL plots are shown in Figure 11, which help to identify which region of the frequency spectrum is more active thereby elucidating what type of flow-field exists in the cavity. As for the clean weapon bay flow analysis, noise level content across four frequency ranges (i.e. $50\ Hz \leq f \leq 250\ Hz$, $350\ Hz \leq f \leq 450\ Hz$, $500\ Hz \leq f \leq 700\ Hz$ and $750\ Hz \leq f \leq 850\ Hz$) are illustrated in Figure 11. These four frequency bands straddle the first four Rossiter modes typically found for the L/D=5 cavity at a free-stream Mach number of 0.85.

For both half-body and full-body missiles, SPLs are at least 10-15 dB lower than the baseline experimental and numerical results for frequencies above 350 Hz. For the baseline case, i.e. where no missile is used, the dominant mode is the third Rossiter mode ($\approx 600\ Hz$). When the missile inserted at the cavity shear layer plane, the intensity of this mode has diminished by as much 60 dB at the cavity rear (Figure 11(c)). The dominant mode has also shifted to the lower end of the frequency spectrum (Figure 11(a)) where the noise levels at the cavity rear are of the same order of magnitude as the baseline experimental and numerical

results. Even with $50\ Hz\ \leq\ f\ \leq\ 250\ Hz$, the flow at the front of the cavity $(x/L = 0.05)$ is significantly quieter than at the rear $(x/L = 0.95)$.

(a) $50\ Hz\ \leq\ f\ \leq\ 250\ Hz$

(b) $350\ Hz\ \leq\ f\ \leq\ 450\ Hz$

(c) $500\ Hz\ \leq\ f\ \leq\ 700\ Hz$

(d) $750\ Hz\ \leq\ f\ \leq\ 850\ Hz$
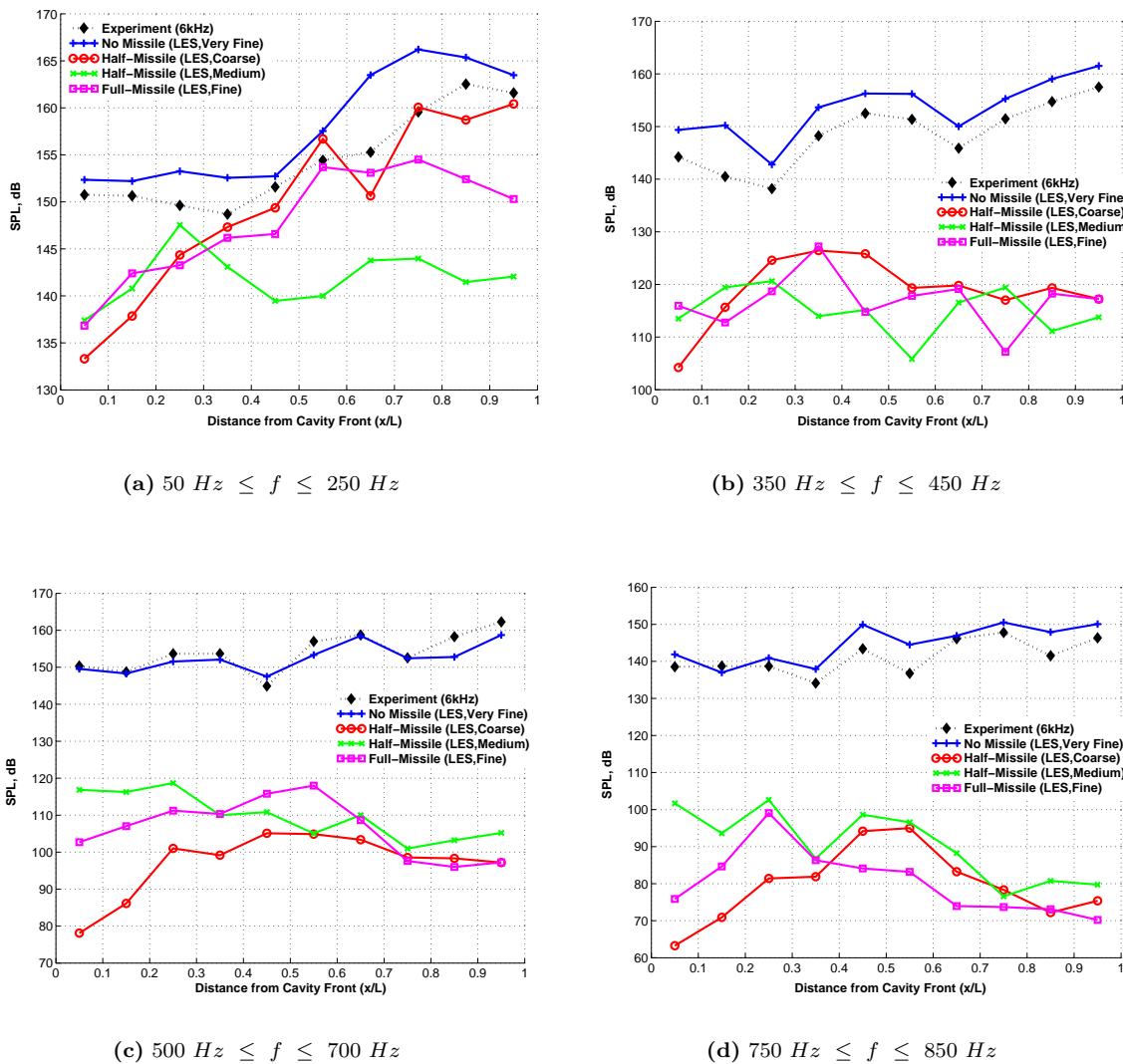
Figure 11: Band-limited SPLs across four frequency ranges along the cavity floor for the 3D, L/D=5, W/D=1 cavity with missile without fins using LES for the coarse and medium half-body missile grids and the fine full-body missile.

The fact that the frequencies within the first range $(50\ Hz\ \leq\ f\ \leq\ 250\ Hz$) are dominant with the missile inserted in the cavity suggests that a wake-like mode is triggered. For the L/D=5 cavity at a free-stream Mach of 0.85, the flow exhibited in the cavity is described as a shear layer mode, where a shear layer forms and spans across the entire cavity opening thereby separating the lower-speed flow inside the cavity from the higher-speed external flow. In the wake mode, the shear layer does not have sufficient energy to span the cavity opening and instead 'rolls up' to form to vortical structures near the cavity front that convect downstream. Vortex shedding prevails in this case and the lower frequencies and their harmonics are more evident. In fact, with the missile placed inside the cavity, frequencies much lower than the first Rossiter mode $(\approx 160\ Hz$) exist and it is these that contain the most energy. Evidence of this is provided in Figure 12 below, which illustrates the noise level content along the cavity floor for frequencies contained within the range $0\ Hz\ \leq\ f\ \leq\ 50\ Hz$. The coarse half-body missile grid produces approximately 12 dB more noise from these lower frequencies at the cavity rear relative to the baseline experiment results. The fact that the full-body missile generates 5-20 dB less noise than the half-body coarse missile also explains why the

half-body missile coarse grid generates greater overall noise (Figure 10(b)). Signal length for the medium half-body missile grid without fins is not currently long enough for any noise content in this lower frequency range to be observed and hence was omitted.
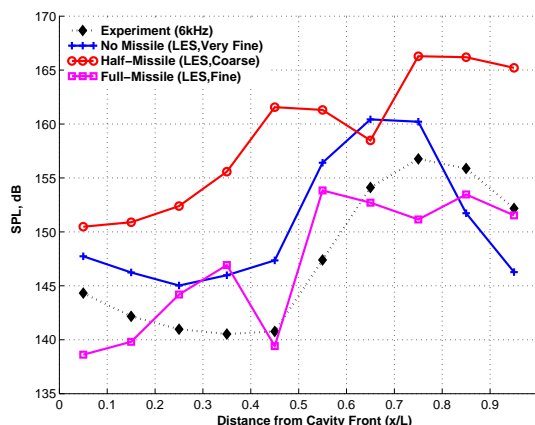
Figure 12: Band-limited SPLs within $0\ Hz\ \leq\ f\ \leq\ 50\ Hz$ along the cavity floor for the 3D, L/D=5, W/D=1 cavity with a missile without fins using LES for the coarse and medium half-body missile grids and the fine full-body missile.

The lower frequencies dissipate more quickly into the environment and cause less damage to the surrounding cavity structure and the store. The effect of the missile (without fins) situated at the shear layer plane therefore appears to pacify the flow inside the cavity shifting the dominance from the higher frequencies to the lower ones. The influence of the missile however is likely to vary depending on where it is located in the cavity as was reported by Baysal *et al.* [15]. This however requires further investigation before more conclusive statements can be made.

Visualisation of the flow-field inside the cavity with the missile without fins placed in the shear layer plane is provided in Figure 13, which illustrates pressure contours with streamlines to show the structures developing inside the cavity. For reference, the flow-field inside the baseline clean cavity without any missile is also shown. All plots are drawn on the same scale and each plot is taken at approximately the same time-step in the flow cycle for direct comparison. Irrespective of whether a half-body or a full-body missile is used, the flow inside the cavity is observed to be more organised compared to the baseline case (Figure 13(a)). The flow in the baseline cavity is reasonably organised in the front of the cavity but becomes chaotic as the shear layer begins to break down. Where the missile is inserted in the cavity, typically a large region of recirculation is generated just aft of the leading edge of the missile. The lower SPLs depicted in Figure 10(b) for the full-body missile suggest that most of the flow is shed downstream rather than being retained within the cavity causing little impingement of the flow with the downstream cavity wall. In contrast, much of the flow for the baseline cavity (Figure 13(a)) impinges on the cavity rear bulkhead. The high pressure that accummulates at the cavity rear manifests itself in the form of a rising SPL curve in Figure 10(b) for the baseline cavity.

The confining presence of the missile body prevents the vortices from moving around inside the cavity. With the missile placed along the shear layer plane, the growth of the shear layer across the cavity opening is also restricted. Consequently, the oscillatory motion of the shear layer is also limited and hence its impingement near the downstream cavity corner avoided. This prevents the creation of acoustical disturbances and high noise levels resulting in a less turbulent flow-field with lower frequencies being more dominant. It is also possible that the curved nose of the missile will further promote shear layer breakdown as the flow will be forced to 'swirl' into the cavity. This results in more of the energy being redistributed from the streamwise and transverse directions into the spanwise direction. Investigations with finer grids will provide more conclusive evidence.

For the missile with fins, initial computations were conducted with the fin geometry slightly modified to

(a) No Missile (t=0.0254s)

(b) Half-Missile (Coarse) Without Fins (t=0.0181s)

(c) Half-Missile (Medium) Without Fins (t=0.0181s)

(d) Full-Missile (Fine) Without Fins (t=0.0181s)
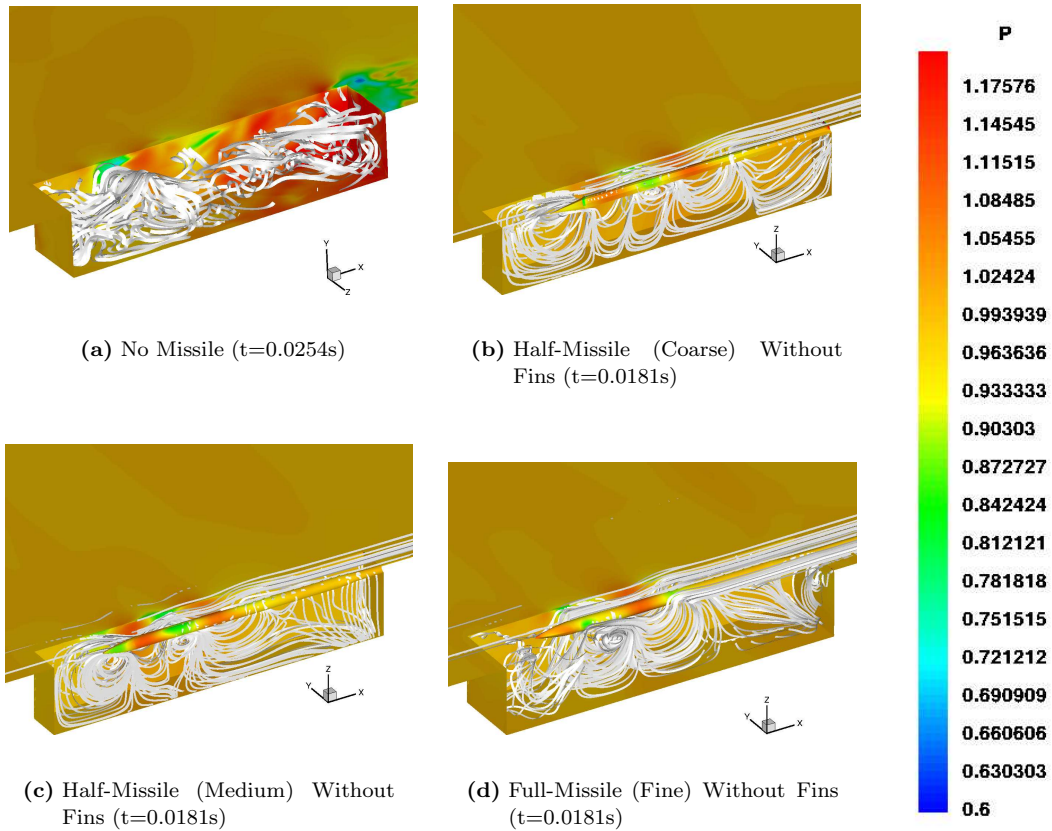
Figure 13: Flow-field visualisation for the clean cavity with and without missile (without fins). Results from both half-model and full-model missiles are presented, where the missile is positioned at the edge of the half-cavity model. Clean cavity results without missile obtained using 8.5 million LES grid.

facilitate running of calculation. The fins evidently add more complexity to the geometry and the grid generation process. Results from a steady-state laminar calculation are presented in Figure 14(b) below. The corresponding meshing distribution on and around the missile with fins is illustrated in Figure 14(a).

(a) Mesh

(b) Flow-field (t=0.0s)
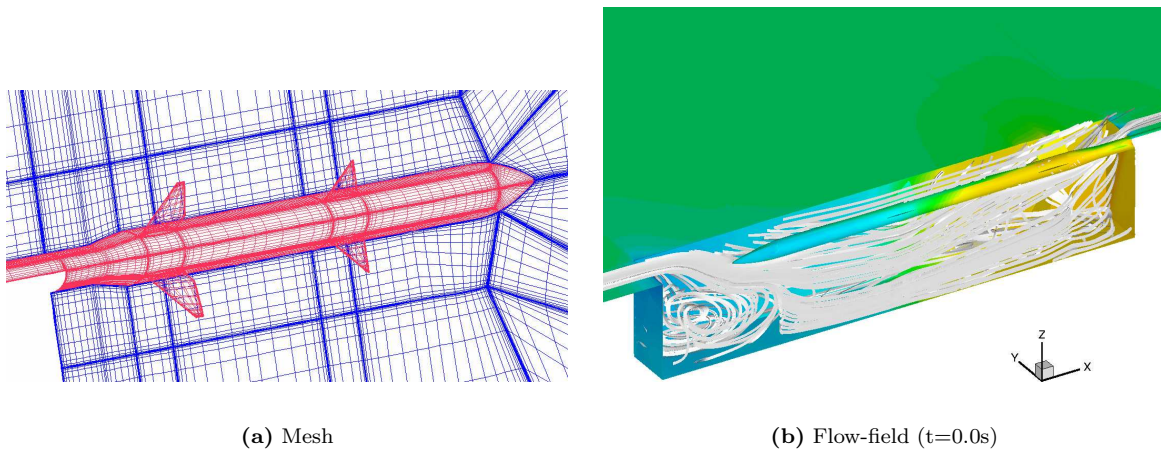
Figure 14: Mesh distribution on and around the half-model missile with fins and flow-field using pressure contours (laminar) inside the cavity with streamlines.

4.3 Flow Control for Weapons Bay

Effectiveness of the spoiler, slanted cavity walls and steady jet blowing as a passive control device were investigated in this study. For each control method, the control device was placed at different locations and its influence recorded. In each case, where no control method is used is denoted as 'baseline'. Although no experimental data was available for this control study, results were compared to the computational 'baseline' case as well as to the corresponding experimental results (i.e. for the clean, 2D, L/D=5 cavity where no control method was used) to illustrate effectiveness of the control method.

Due to the reasonable predictive capability of the SST turbulence model on coarse grids based on previous analyses and the requirement for low computational run-time, all computations performed in this control study used the SST model only. In this manner, turbulence modelling issues were minimised and any changes in the cavity flow can reasonably accurately be assumed to be predominantly dependant on the control method employed. Table 3 provides description of all the grids used for the control studies.

Grid Type	Pts. in Cavity (Overall)	Wall-Spacing	Blocks in cavity (Overall)
2D L/D=5 clean cavity			
Coarse	10,302 (33,250)	1.05×10^{-5}	1 (6)
2D L/D=5 cavity with spoiler			
LE Spoiler (Case 1)	10,200 (80,658)	5×10^{-6}	2 (17)
LE Spoiler (Case 2)	22,800 (150,450)	5×10^{-6}	2 (17)
TE Spoiler (Case 3)	10,200 (65,860)	5×10^{-6}	2 (15)
2D L/D=5 cavity with slanted walls ($\theta = 45^\circ$)			
Slanted Front Wall	11,016 (35,394)	5×10^{-6}	2 (8)
Slanted Rear Wall	9,894 (31,212)	5×10^{-5}	2 (8)
Slanted Front & Rear Walls	10,302 (31,926)	7×10^{-5}	1 (6)
2D L/D=5 cavity with steady jet blowing ($M_j = 0.1M_\infty$)			
Front Wall Jet	25,654 (46,972)	5×10^{-6}	4 (9)
Rear Wall Jet	25,856 (47,174)	5×10^{-6}	4 (9)
Upstream Jet	30,408 (103,178)	5×10^{-6}	6 (24)

Table 3: Information about the grids used for the 2D, L/D=5, clean cavity control study.

4.3.1 Spoiler

The position of the spoiler relative to the cavity was varied and its effect on the cavity acoustics and flow structures studied. The width (w_{sp}) and height (h_{sp}) of the spoiler was kept fixed at 0.25 inches and 0.42 inches (which is approximately equal to the height of the boundary layer, δ), respectively. Details of the grids used in this case are provided in Table 3. For clarity, the three different spoiler configurations are denoted as Cases 1, 2 and 3. Case 1 denotes the LE spoiler whose co-ordinates correspond to $x_{sp}/L = -0.2, y_{sp}/L = 0$, Case 2 for the LE spoiler with co-ordinates $x_{sp}/L = -0.1, y_{sp}/L = 0$ and Case 3 for the TE spoiler with co-ordinates $x_{sp}/L = 1, y_{sp}/L = 0$. A schematic of the different spoiler positions and appropriate dimensions is illustrated below in Figure 15.

Pressure traces for all the different spoiler positions at the cavity rear ($x/L = 0.95$) along the cavity floor as well as SPLs are illustrated in Figure 16 below. Numerical and experimental results for the 'baseline' case (i.e. with no spoiler) are also indicated for reference.

Generally, the upstream spoiler produces less noise inside the cavity. For the LE spoiler located furthest upstream (Case 1), denoted by a red line with circular symbols, pressure amplitudes are completely damped out resulting in a drop in the SPLs by as much as 30 dB from experiment. This results in a flat SPL curve (Figure 16(b)) and is indicative of frequencies being damped out. As the spoiler is moved closer to the front corner (Case 2a), more noise is generated at the cavity rear ($x/L = 0.95$) as is indicated by the peaks in the
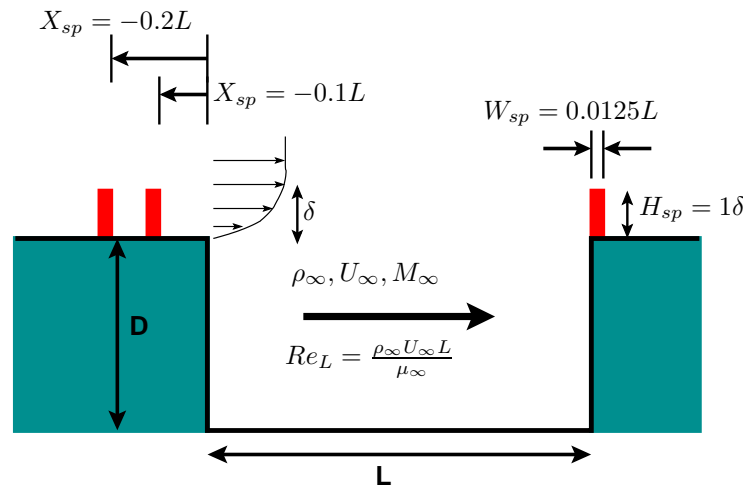
Figure 15: Schematics of the spoiler at different positions.

SPL curve at about $x/L = 0.15$ and $x/L = 0.9$, respectively. Variations in the pressure signal are therefore greater at these locations as the spoiler is moved closer to the front. These fluctuations are however much smaller than the experimental pressure oscillations and so the pressure signal appears flat for the scale drawn in Figure 16(a). Noise levels are consequently slightly higher for this case relative to the spoiler furthest upstream (Case 1) by about 5 dB but this is still about 25 dB lower than experiment at the cavity rear ($x/L = 0.95$).

(a) Pressure Traces ($x/L = 0.95$)   **(b)** SPLs
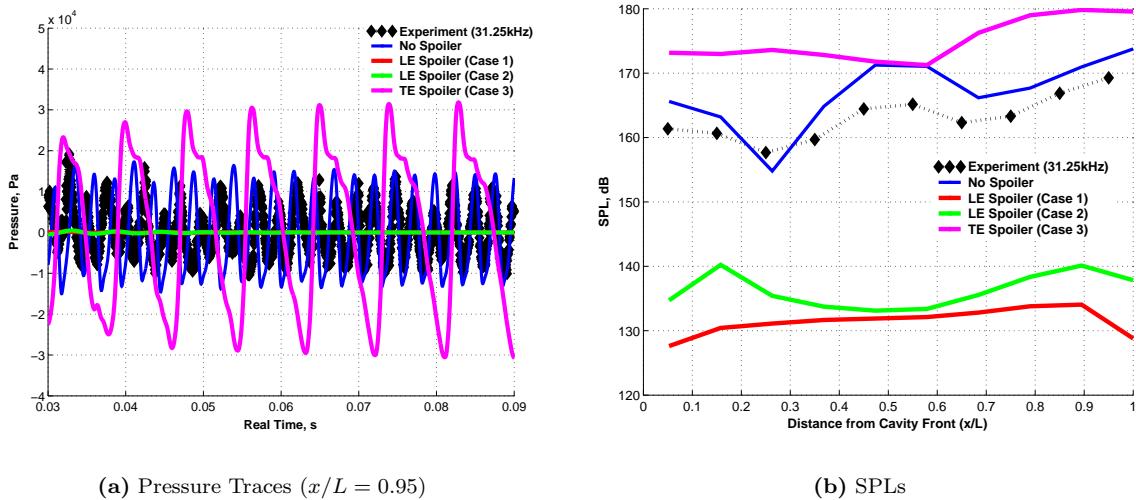
Figure 16: Pressure traces (at $x/L = 0.95$) and SPLs along cavity floor of the 2D, L/D=5 cavity using the SST turbulence model with: LE Spoiler (Case 1), LE Spoiler (Case 2), TE Spoiler (Case 3). CFD and experimental results with no spoiler also included.

When the spoiler is placed at the downstream cavity corner (Case 3), pressure amplitudes increase more significantly resulting in an increase in the overall noise levels generated at the cavity floor by as much as 6-7 dB at the cavity rear (Figure 16(b)). Wavelengths of the pressure oscillations (denoted by magenta lines with square symbols) for the trailing-edge spoiler are found to be greater than compared to experiment and suggests that lower frequencies are more dominant. This dramatic change in the periods of the frequencies appears to suggest that the wake mode has been activated as was encountered in previous computations.

Illustration of the flow-field inside the cavity with the spoiler is shown in Figure 17, which displays time-

averaged plots with Mach contours and streamlines. For reference, flow-field inside the cavity without a spoiler is also included (Figure 17(a)). Analysis of the flow-field plots for the LE spoilers (Cases 1 and 2a) clearly indicate that the spoiler forces the flow to separate ahead of the normal separation point at the cavity lip (see Figure 17(a)), deflecting the flow upwards. Momentum of the free-stream then 'carries' this prematurely-separated flow further downstream. Although a shear layer still forms across the cavity opening, it is now shifted upwards and the flow re-enters the cavity tangentially to the downstream wall, i.e. flow enters vertically from the transverse direction (Figures 17(b) and 17(c)). Flow is therefore observed to graze along the downstream wall rather than impinge against it. In contrast, the shear layer approaches the cavity rear for the baseline case in the streamwise direction and therefore impacts the downstream wall almost perpendicularly (Figure 17(a)). The mass breathing process that would normally initiate injection and ejection of fluid in and out of the cavity due to the deflection of the shear layer is thus eliminated and generation of acoustical disturbances (and subsequent propagation of acoustic waves) minimised. In this manner, higher frequencies are also eliminated.

(a) No Spoiler

(b) LE Spoiler (Case 1)

(c) LE Spoiler (Case 2)

(d) TE Spoiler (Case 3)
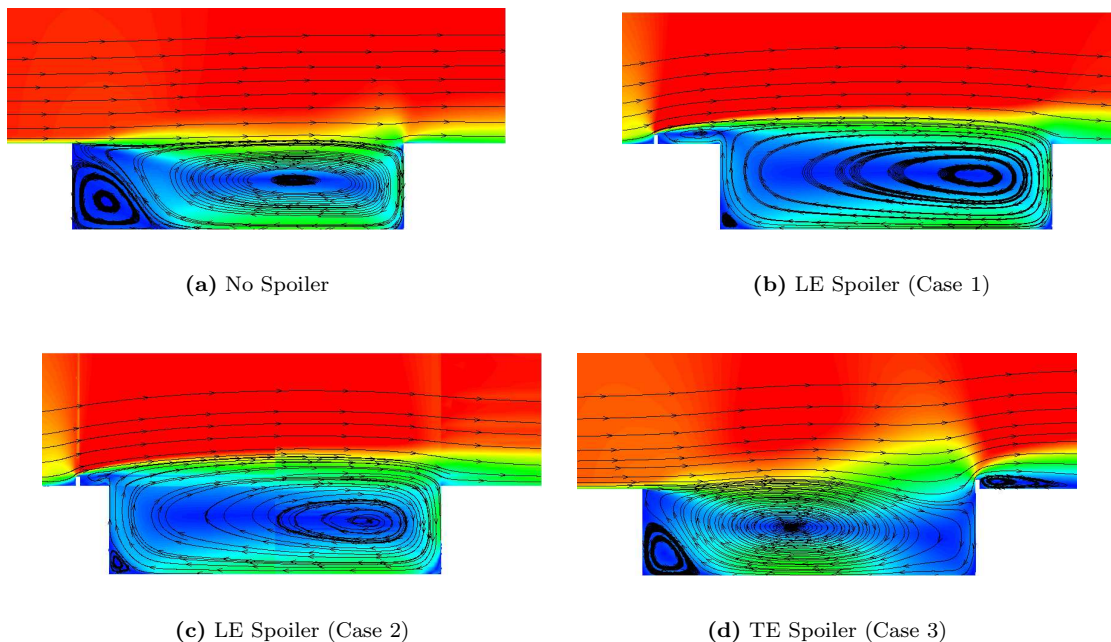
Figure 17: Time-averaged Mach contours with streamlines using the SST model for the 2D, L/D=5 cavity with the spoiler upstream and downstream of cavity (see Figure 15). All plots use Mach number normalised with reference to the free-stream Mach number, $M_\infty = 0.85$.

By changing the position of the spoiler from upstream to downstream of the cavity, the physics of the flowfield inside the cavity changes completely. For the trailing-edge spoiler, the shear layer mode no longer exists as it does for the case without the spoiler (Figure 17(a)). Instead, vortex shedding occurs at the cavity lip and the flow switches to the wake mode (Figure 17(d)). It was found that the trailing-edge spoiler decelerates a larger proportion of the oncoming free-stream air thereby creating a region of very high pressure at the cavity rear. Near the cavity front, the flow separates at the cavity lip and rolls into the cavity. The high pressure region at the cavity rear, however, prevents the vortex from convecting any further downstream. As a result, the vortex is forced to expand outwards of the cavity. This large vortex forces more flow to deflect around it and moves the separation point ahead of the cavity further upstream. This results in another vortex that rolls into the cavity and a continuous vortex-shedding cycle that generates the large pressure oscillations inside the cavity as illustrated in Figure 16. Large peripheral velocities of the vortices (depicted by the lighter, higher Mach regions in Figure 17(d)) near the cavity floor are responsible for more intense shearing of the vortex with the walls and hence causes noise levels much higher than experiment and even the baseline case (Figure 16(b)).

4.3.2 Slanted Cavity Walls

For the slanted cavity walls, the different slopes investigated are illustrated in the schematic in Figure 18. Details of the grids used for each of these cases are provided in Table 3. Three different scenarios were investigated: slanting the front cavity wall only, slanting the rear cavity wall only and slanting both front and rear walls. The angle of slant was kept fixed at 45° in all these cases.
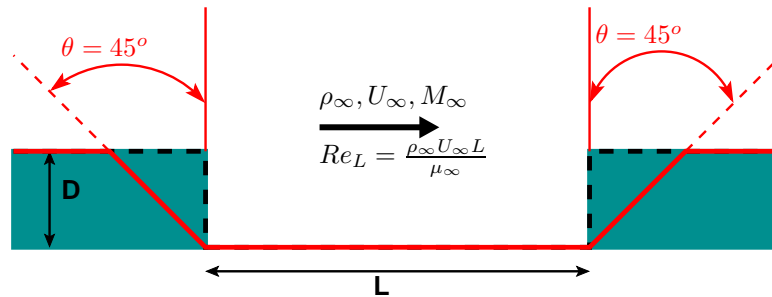
Figure 18: Schematic of cavity walls slanted at different positions.

Figure 19 below plots the SPLs and pressure traces (at $x/L = 0.95$) for a slanted front wall (red with circular symbols), slanted rear wall (green with crosses) and both walls slanted (magenta with square symbols). Experimental (black with diamond symbols) and numerical (blue with plus signs) results corresponding to the baseline case where no slant was implemented are also included for demonstration of the effectiveness of the control method.

(a) Pressure Traces ($x/L = 0.95$)   **(b)** SPLs
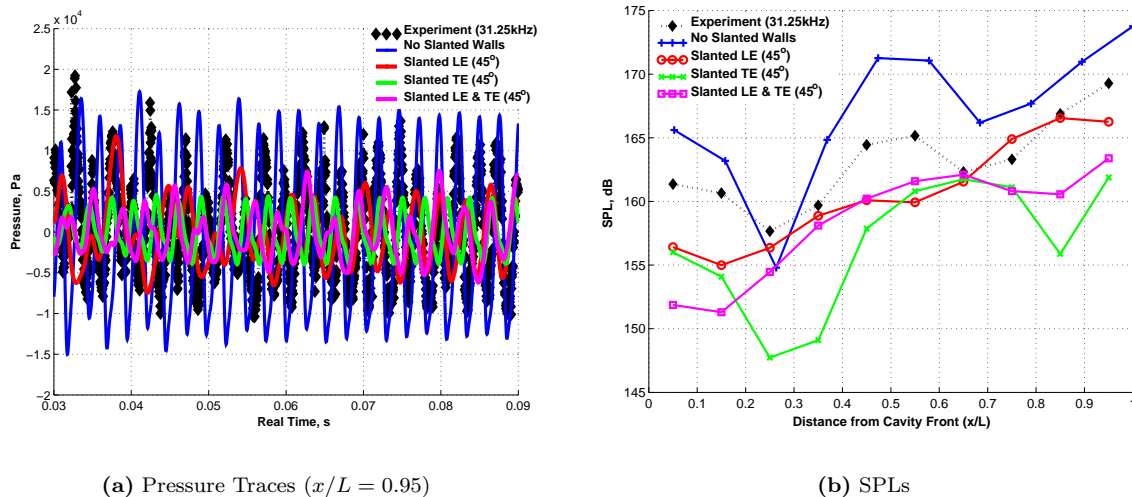
Figure 19: Pressure traces (at $x/L = 0.95$) and SPLs along cavity floor for the 2D, L/D=5 cavity using the SST turbulence model for slanted front wall, slanted rear wall and both walls slanted. Slant angle fixed at 45° .

As far as mitigating the intensity of noise is concerned, slanted walls, irrespective of position, appear to be an effective method with maximum pressure amplitudes generally tending to be lower than those given by experiment or numerically for the baseline case. Slanting only the front wall however appears to be the least effective of all the three cases investigated with noise levels significantly higher at around the x/L=0.25 and x/L=0.75 positions. The 'dips' in the SPL curve, which are approximately coincident to the average locations of the cores of the vortices, are also damped out (Figure 19(b)). Slanting the downstream wall produces greater reductions in SPLs throughout the cavity length (by $\approx$ 5-12 dB). Slanting both front and rear walls appears to be quieter at the rear ($x/L = 0.95$) while the rest of the noise level distribution (especially along

the cavity middle section) resembles the slanted front wall only results.

Illustrations of the time-averaged flow-field inside the cavity for different slanted wall configurations are provided in Figure 20 below. Plots contain streamlines superimposed on Mach contours normalised with respect to the free-stream Mach number, $M_\infty = 0.85$. Boundaries and thicknesses of the shear and boundary layers are clearly defined in this manner as is the degree of flow intensity inside the cavity. For reference, the flow-field with no walls slanted is also included (Figure 20(a)). Irrespective of which wall is slanted, the front wall corner vortex has largely disappeared. The high Mach region along the cavity floor (distinctly evident from the lighter, green Mach contours) extends across a greater proportion of the cavity length. Noise generated on the cavity floor is therefore more distributed. Overall noise levels are however only significantly lower when the rear wall is slanted (Figure 20(c)). When the front wall is slanted (Figure 20(b)), SPLs are still of the same magnitude as that of experiment and the numerical results with no slant used (Figure 19(b)). This suggests that moving the position of the front corner further upstream (while keeping the L/D ratio of the cavity fixed) can cause adverse effects. Changing the angle of both walls merely combines the adverse effects of slanting the front wall and the positive effects of slanting the rear wall to give a compromised solution (Figure 20(d)).

(a) No Slanted Walls

(b) Slanted Front Wall (45°)

(c) Slanted Rear Wall (45°)

(d) Slanted Front & Rear Walls (45°)
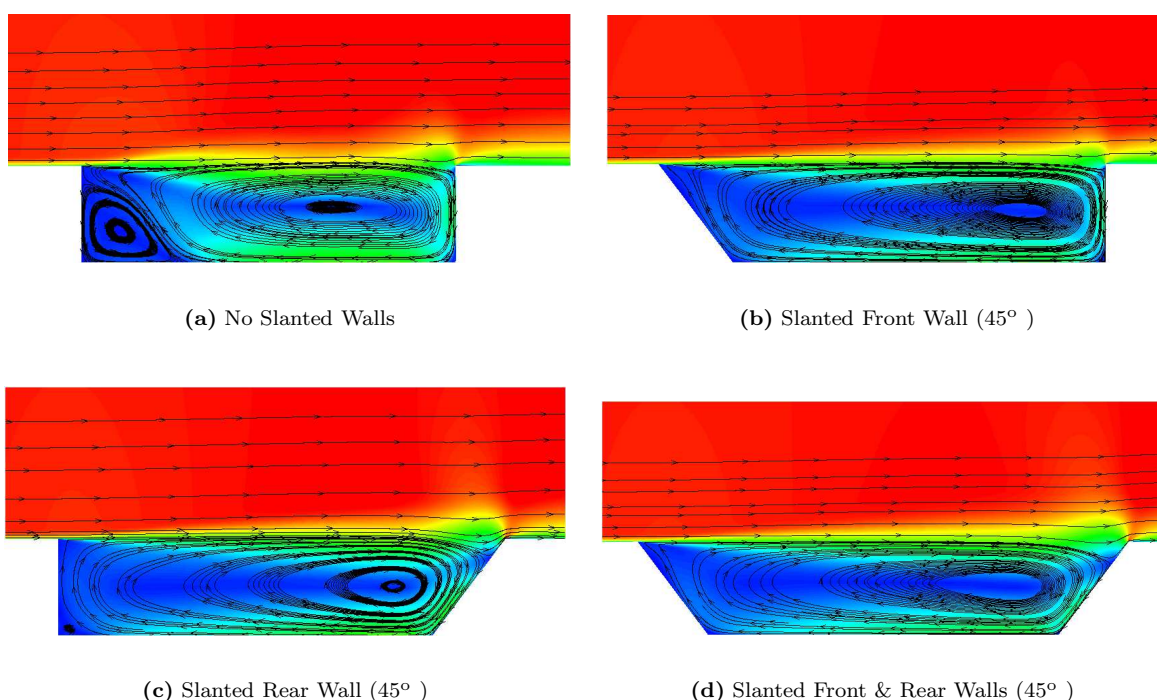
Figure 20: Time-averaged Mach contours with streamlines using the SST model for the 2D, L/D=5 cavity with slanted front wall, slanted rear wall and both walls slanted. Angle of slant kept fixed at 45° .

The downstream corner is also naturally located further downstream as a consequence of slanting the cavity back wall. This forces the shear layer and any flow structures created to remain almost completely entrained within the cavity and thus the mass breathing process is minimised. Furthermore, with the rear wall slanted at 45° , the geometrical surface area of the downstream wall has increased by a factor of $\sqrt{2}$. Stress generated by the shearing of the vortex with the walls is therefore more distributed. Consequently, the noise levels generated at the cavity rear are much lower (by $\approx$ 7 dB) compared to experiment (see Figure 19(b)). Containment of the flow within the confinements of the cavity walls makes the flow intrinsically less unsteady. Vortical movement and shear layer deflection is minimised as a result. When both the front and rear walls are slanted, flow features are an amalgamation of the individually slanted front and rear walls. At the front, the streamwise velocity trace is therefore similar to the slanted front wall only and at the cavity rear it resembles the slanted rear wall only results.

4.3.3 Steady Jet Blowing

The final control method analysed here involves steady jet blowing, which endeavours to influence the flow in the cavity by blowing additional air into it. The basic concept of the steady jet is taken from Lamp & Chokani[16] where the jet exit velocity is calculated based on a reservoir total pressure and total temperature, assuming isentropic conditions. The angle of the jet here has been fixed to be perpendicular to the flow. For each case presented, the jet exit Mach number is set to $0.1M_\infty$. With a total reservoir pressure and temperature of 2 atmospheres and 298 K respectively, the jet exit velocity was calculated to be 29.4 m/s. The jet slot width, w_j, was also kept fixed at 0.02L. For this case, the blowing co-efficient, C_μ, derived as the ratio of the exit jet to the free-stream mass flow rate, comes to 0.005. With these jet configurations, computations with three different jet locations were conducted: upstream (i.e. jet located ahead of cavity front corner $[x_j/L = -0.02, y_j/L = 0]$), front wall (i.e. jet located at $[x_j/L = 0, y_j/L = -0.02]$) and rear wall (i.e. jet located at $[x_j/L = 1, y_j/L = -0.02]$). A schematic of the different jet positions is depicted in Figure 21.
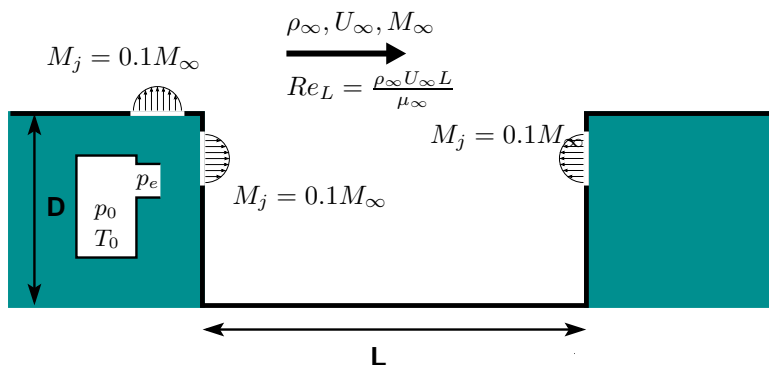
Figure 21: Schematic of the jet (with steady blowing) at different positions.

In all jet locations, pressure oscillations and frequencies experienced in the baseline case were damped out with steady jet blowing and the flow became steady. This is illustrated in Figure 22, which shows the SPLs and pressure traces for the jet located upstream (red line with circular symbols), jet located at the front cavity wall (green line with crosses) and jet located at the downstream cavity wall (magenta line with square signs). For reference, experimental (black line with diamond symbols) and numerical (blue with plus signs) results corresponding to the baseline case without any jet are also included.

The reason why the jet is so effective in controlling the self-sustained oscillations inside the cavity can be illustrated using the time-averaged Mach contour plots in Figure 23. With the jet located at the front wall 23(c), the jet simply adds more momentum to the shear layer. The extra momentum ensures that the shear layer entirely bridges the cavity opening and minimises the extent to which energy is transferred from the shear layer to within the cavity. Acoustical disturbances caused by the impingement of the flow at the cavity downstream wall are therefore eliminated. Consequently, the pressure waves and hence the self-sustained pressure oscillations that drive the flow cycle are cancelled out. The flow becomes steady and the typical dual-vortex cycle with large shear layer deflection as observed in the baseline case (Figure 23(a)) becomes a single, static vortex with no shear layer deflection with steady jet blowing (Figure 23(c)).

In contrast, the rear wall jet extracts momentum from the shear layer causing it to decelerate and diffuse. This diffused shear layer is clearly evident from the larger cross-sectional area of the flow shed downstream of the cavity in Figure 23(d). Comparisons of SPLS between the front wall and rear wall jet reveals that the rear wall jet produces significantly more noise. The greater region of higher Mach numbers depicted by the lighter, green colours in Figure 23(d) is indicative of the greater shear between the vortices and the cavity floor and hence greater noise.

For the upstream jet, where the jet is fired vertically upwards, momentum is added to the transverse component rather than the streamwise component as was the case with the front wall jet. Shear layer is therefore
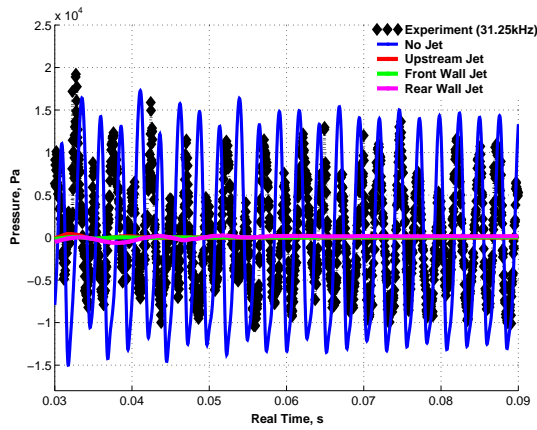
(a) Pressure Traces ($x/L = 0.95$)
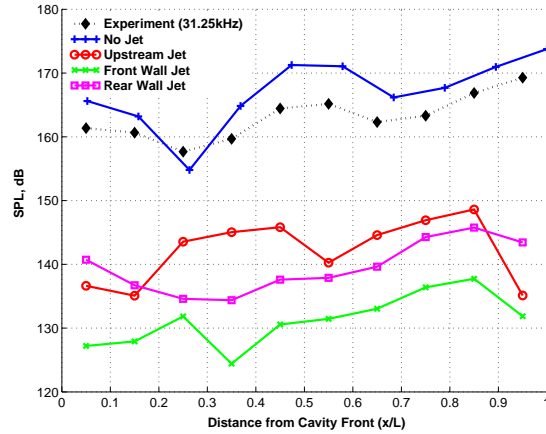
(b) SPLs

Figure 22: Pressure traces (at $x/L = 0.95$) and SPLs along cavity floor for the 2D, L/D=5 cavity using the SST turbulence model with steady jet blowing applied upstream of cavity, at front wall and at rear wall.

(a) No Jet

(b) Upstream Jet

(c) Front Wall Jet

(d) Rear Wall Jet
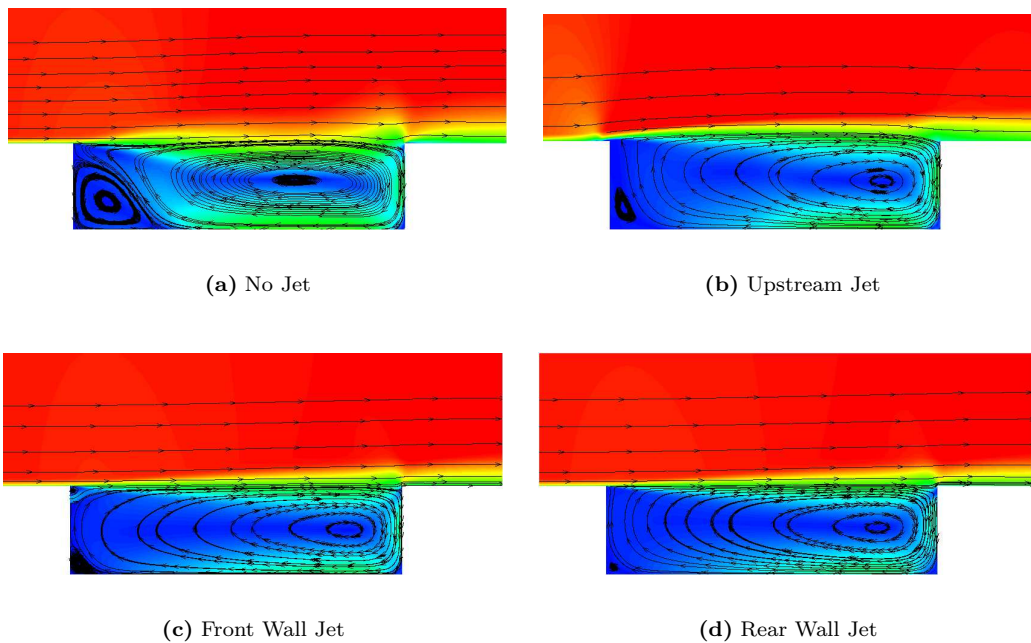
Figure 23: Time-averaged Mach contours with streamlines inside the 2D, L/D=5 cavity using the SST turbulence model with steady jet blowing applied upstream of cavity, at front wall and at rear wall.

forced to detach further upstream of the cavity and its curved trajectory creates a more favourable pressure gradient that accelerates the flow over it (Figure 23(b)). With the shear layer inclined at an angle and having more energy, it redistributes its momentum into the cavity. Vortices of larger circulation strength are therefore created as depicted by the region of stronger Mach number at the rear of the cavity floor in Figure 23(b) compared to other jet locations. Higher peripheral vortex velocities at the cavity floor therefore lead to the higher noise levels inside the cavity for the upstream jet (Figure 22(b)). As the shear layer is redirected by the upstream jet, impingement of the shear layer with the cavity rear wall is again negated

and the self-sustained pressure oscillations are attenuated. The result is therefore a steady solution (Figure 22(a)) and a single-vortex structure presides inside the cavity (Figure 23(b)).

5   CONCLUSIONS

Analysis and control of weapon bays modelled by a 3D cavity with L/D=5 and W/D=1 are presented. All computations with a free-stream Mach of 0.85 and a Reynolds number of 6.783 million using the PMB code developed by University of Glasgow. Analysis of clean weapon bays are first presented where results from URANS, LES and DES are compared. The effect of a store on the cavity flow-field is then illustrated and the paper is concluded by demonstrating the effectiveness of passive control methods to alleviate the high noise levels and frequencies generated in the 2D, L/D=5 clean weapon bay.

Analysis of unsteady pressure measurements with experiment revealed that both DES and LES consistently gave better agreement than URANS in terms of both frequency content, phase and noise levels for both the doors-on and doors-off configurations. Menter's Baseline $k - \omega$ model was also run for this 3D cavity with and without doors but had difficulty in capturing most of the higher (and in some cases, some of the lower) frequencies in both cases. For the doors-off case, Menter's Baseline $k - \omega$ model still predicted a 'W'-shaped SPL curve as it did for the doors-on case unlike LES and DES, which correctly predicted the shape of the SPL curve. Flow-field visualisation for the doors-off cavity with Menter's Baseline $k - \omega$ model and DES revealed that DES predicted a breakdown of the shear layer while Menter's baseline $k - \omega$ model consistently illustrated a coherent shear layer that spanned the cavity. It was concluded that URANS had difficulty in accounting for the larger transport and/or diffusion of energy and momentum present in the doors-off case.

Streamwise and transverse velocity plots were compared for the doors-on case with PIV measurements and showed consistently good agreement at the cavity front and middle for different DES variants and LES. At the cavity rear, the agreement with PIV deteriorated and these discrepancies may be attributed to poor resolution in the PIV experiment at this position.

Numerical analysis of the flow-field inside the cavity (without doors) influenced by the presence of a store placed along the shear layer plane is also investigated. Comparisons were made with experiment corresponding to the cavity without missile to illustrate the effect of the missile on the flow-field. Results for the missile without fins showed that the flow inside the cavity is more organised with lower frequencies appearing to be more dominant, which are less detrimental to the surrounding structure and dissipate quickly into the environment. The use of a symmetry plane along the cavity longitudinal axis appears to be unjustified and leads to spurious results as it over-predicts the noise levels produced inside the cavity. Further studies will use refined grids to analyse the flow around the missile with and without fins. The effect of doors on the cavity flow-field with a missile as well as different positions of the missile inside the cavity will also be investigated.

Calculations with different passive control methods with the 2D, L/D=5 cavity were conducted in the aim of reducing the high noise levels and large frequency content observed inside the cavity. Effectiveness of the spoiler, slanted cavity walls and steady jet blowing as a passive control method was investigated. For the spoiler, reductions in SPLs of about 30 dB were achieved when the spoiler was placed upstream of the cavity but overall noise levels increased when the spoiler is placed aft of the cavity. With slanted cavity walls, slanting the front wall induced massive separation at the front corner and maintained relatively high noise levels inside the cavity. When the rear wall is cavity flow environment is improved and a noise level reduction of about 10 dB can be achieved. Steady jet blowing was found to be the most effective of all passive control methods. Although jets fired from different positions all completely suppressed all acoustic tones making the flow steady, the front wall jet proved to be the most effective obtaining noise level reductions of up to 35 dB.

6   ACKNOWLEDGEMENTS

LIST OF REFERENCES

[1] J.E. Rossiter. Wind Tunnel Experiments on the Flow Over Rectangular Cavities at Subsonic and Transonic Speeds. Technical Report 64037, Royal Aircraft Establishment, October 1964.

[2] R.L. Stallings Jr. Store Separation from Cavities at Supersonic Flight Speeds. *Journal of Spacecraft and Rockets*, 20(2):129–132, March-April 1983.

[3] A.B. Blair Jr and R.L. Stallings Jr. Cavity Door Effects on Aerodynamic Loads of Stores Separating from Cavities. *Journal of Aircraft*, 26(7):615–620, July 1989.

[4] F.J. Wilcox Jr. Experimental Measurements of Internal Store Separation Characteristics at Supersonic Speeds. NASA Technical Report.

[5] D.P. Rizzetta and M.R. Visbal. Large-Eddy Simulation of Supersonic Cavity Flowfields Including Flow Control. *AIAA*, 41(8):1438–1443, August 2003.

[6] P.R. Spalart. Strategies for Turbulence Modelling and Simulations. *International Journal of Heat and Fluid Flow*, 21(3):252–263, June 2000.

[7] J.A. Ross and J.W. Peto. The Effect of Cavity Shaping, Front Spoilers and Ceiling Bleed on Loads Acting on Stores, and on the Unsteady Environment Within Weapon Bays. Technical report, QinetiQ, March 1997.

[8] L. Cattafesta, D. Williams, C. Rowley and F. Alvi. Review of Active Control of Flow-Induced Cavity Resonance. In *33rd AIAA Fluid Dynamics Conference*. AIAA, June 2003. AIAA Paper 2003-3567.

[9] K.J. Badcock, B.E. Richards and M.A. Woodgate. Elements of Computational Fluid Dynamics on Block Structured Grids Using Implicit Solvers. *Progress in Aerospace Sciences*, 36:351–392, 2000.

[10] J.A. Ross. PIV Measurements of the Flowfields in an Aerodynamically Deep Cavity, May 2002. Private Communication.

[11] F.R. Menter. Two-Equation Eddy-viscosity Turbulence Models for Engineering Applications. *AIAA*, 32(8):1598–1605, August 1994.

[12] M. Strelets. Detached Eddy Simulation of Massively Separated Flows. In *39th AIAA Aerospace Sciences Meeting*. AIAA, January 2001. AIAA Paper 2001-0879.

[13] P. Batten, U. Goldberg and S. Chakravarthy. Sub-Grid Turbulence Modeling for Unsteady Flow with Acoustic Resonance. In *38th AIAA Aerospace Sciences*. AIAA, January 2000. AIAA Paper 00-0473.

[14] P. Nayyar, D. Lawrie, G.N. Barakos, K.J.Badcock, and B.E. Richards. Numerical Study of Transonic Cavity Flows Using Large-Eddy and Detached-Eddy Simulation. In *RAeS Aerospace Aerodynamics Research Conference*, London, UK, September 2004. Royal Aeronautical Society.

[15] O. Baysal, K. Fouladi, R.W. Leung, and J.S. Sheftic. Interference Flows Past Cylinder-Fin-Sting-Cavity Assemblies. *Journal of Aircraft*, 29(2):194–202, March-April 1992.

[16] A.M. Lamp and N. Chokani. Computation of Cavity Flows with Suppression Using Jet Blowing. *Journal of Aircraft*, 34(4):545–551, July-August 1997.